Research Square

Preprints are preliminary reports that have not undergone peer review.
They should not be considered conclusive, used to inform clinical practice,
or referenced by the media as validated information.

Framework Zn Modulation of Confined Cu_xO_y Species for Photothermal Methane to Methanol

Wenting Wu

wuwt@upc.edu.cn

China University of Petroleum (East China) https://orcid.org/0000-0002-8380-7904

Jinchen han

Taiyuan University of Technology

Haonan Zhang

State Key Laboratory of Heavy Oil Processing, China University of Petroleum, Qingdao 266580

Yan Sun

Efficiency and Low Carbon Technology

Yue Zhao

Taiyuan University of Technology

Chunlei Sun

Taiyuan University of Technology

Lei Liu

Shanxi Key Laboratory of Chemical Product Engineering, College of Chemistry and Chemical Engineering, Taiyuan University of Technology, Taiyuan, China https://orcid.org/0000-0003-2027-4271

Qiwen Sun

Efficiency and Low Carbon Technology

Zhijun Zuo

Taiyuan University of Technology

Article

Keywords:

Posted Date: July 15th, 2026

DOI: https://doi.org/10.21203/rs.3.rs-10285334/v1

License: This work is licensed under a Creative Commons Attribution 4.0 International License.
Read Full License

Additional Declarations: There is **NO** Competing Interest.

Abstract

Copper exchanged SSZ-13 zeolites are effective catalysts for the photothermal conversion of methane to methanol at low temperatures. Further progress is limited by the difficulty in controlling the structure and dynamic evolution of confined Cu_xO_y active sites. Here we show that framework incorporated Zn in SSZ-13 enables continuous photothermal catalytic methane oxidation, while Zn itself remaining redox inactive. Combined spectroscopic analyses and theoretical calculations reveal that Cu species are confined within the zeolite cages as Cu_2O_2 and Cu_3O_3 clusters. Framework Zn induces interfacial charge transfer from Cu to the Zn modified framework, preferentially stabilizing larger Cu_3O_3 motifs within the eight membered ring cages and markedly lowering the energy barriers for C-H bond activation. Light does not directly initiate methane activation. Instead, it regulates thermal catalysis by modulating the electronic structure and population of Cu_xO_y species, thereby promoting the formation of key reactive intermediates (•OH, $•O_2^-$, and $•CH_3$). As a result, Cu/Zn-SSZ-13 delivers a methanol yield of 466.8 μmol g^{-1} h^{-1} with 79.1% selectivity and maintains stable performance over 100 h, corresponding to a 1.6-fold improvement over conventional Cu/SSZ-13 under purely thermal conditions. This work establishes a framework enabled photothermal strategy for rationally regulating confined metal-oxo species in zeolite catalysts.

Introduction

Selective oxidation of methane to value added oxygenates under mild conditions remains a long-standing challenge in catalysis, owing to the inertness of the C-H bond and the propensity for overoxidation [1–2]. Copper exchanged zeolites, particularly those with CHA topology, have emerged as promising platforms for methane activation because their confined environments can stabilize multinuclear Cu_xO_y species capable of C-H bond cleavage [3–6]. Despite substantial progress, the identity of the catalytically relevant Cu_xO_y motifs and effective strategies to regulate their speciation under reaction conditions remain intensely debated [7–10]. In particular, precise control over the structure, electronic properties, and dynamic evolution of confined Cu active sites is still lacking, limiting further improvements in activity and selectivity.

Introducing secondary elements has been explored to tune Cu zeolite catalysts, yet the roles of such additives are often poorly defined [11–12]. In many cases, heteroatoms or promoters are assumed to act as redox active species or surface modifiers, which can lead to particle formation, pore blockage, or undesired side reactions [11, 13–15]. Consequently, a fundamental question remains unresolved: can a secondary element be rationally incorporated into the zeolite framework to modulate the structural and electronic evolution of confined Cu_xO_y species without directly participating in methane activation chemistry? Addressing this question requires disentangling confinement effects from electronic interactions and establishing design principles that go beyond empirical promoter effects.

Herein, we demonstrate that framework incorporated Zn in Chabazite (CHA) zeolites enables a continuous photothermal catalytic evolution of confined Cu_xO_y species during methane oxidation. Unlike conventional bimetallic systems, Zn does not serve as a redox active site; instead, it functions as a photonic and electronic modulator that induces charge transfer and stabilizes larger Cu_3O_3 motifs within the zeolite cages under oxidative conditions. Combining spectroscopic characterization, kinetic analysis, and density functional theory (DFT) calculations, we show that light does not directly initiate methane activation but rather regulates thermal catalysis by reshaping the electronic structure and population of Cu active sites. This framework enabled photothermal strategy offers a general conceptual approach for regulating confined metal-oxo species in zeolite catalysts.

Results and Discussion

Zn-SSZ-13 was synthesized via a one pot hydrothermal route by introducing a Zn source into the initial synthesis gel to partially substitute framework T sites [16–17], followed by light assisted Cu ion exchange to obtain Cu/Zn-SSZ-13. This synthetic protocol ensures that Zn is embedded within the CHA framework rather than existing as extra framework species or surface modifiers. Under light irradiation, electrons transfer from the molecular sieve to zinc, then zinc becomes more electron-rich and can selectively adsorb more copper [18], thereby promoting the selective formation of Cu oxides on zinc.

Powder X-ray diffraction (XRD) confirms that all samples retain the CHA topology (Fig. 1a). However, Zn containing materials display a systematic shift of diffraction peaks toward lower 2θ values, indicating framework expansion induced by Zn substitution [17, 19–24]. Figure 1b presents the comparative ^{29}Si solid state MAS NMR spectra of the parent SSZ-13 and the Zn incorporated Zn-SSZ-13. In the spectrum of the unmodified SSZ-13, two typical resonance signals can be observed, which are assigned to the conventional Si-O-Si coordination environment and the Si-O-Al coordination environment within the zeolite framework [25]. Notably, in the spectrum of the Zn-SSZ-13 sample, alongside the preservation of the original aluminosilicate framework signals, a distinct new characteristic resonance shoulder peak (Si-O-Zn) emerges between the Si-O-Si and Si-O-Al peaks. This peak directly confirms the formation of Si-O-Zn linkages within the zeolite framework [26]. This alteration in the chemical shift provides direct, atomic level spectroscopic evidence compellingly demonstrating that the introduced Zn species do not exclusively exist as free oxides or isolated extra framework ions within the zeolite channels. Instead, a portion of Zn is successfully incorporated into the topological framework of SSZ-13 via isomorphous substitution, thereby altering the local chemical microenvironment of the adjacent silicon atoms (Fig. 1c). The HAADF-STEM image in Fig. 1d reveals that copper species are present as clusters (Figure S1). DFT calculations were then performed to elucidate the detailed structure of these clusters.

Consistently, Fourier transform infrared spectroscopy (FT-IR) shows a slight distortion of the T-O-T asymmetric stretching band centered at 1215 cm^{-1} upon Zn incorporation (Figure S2), suggesting modification of the framework bonding environment [27–29]. UV-vis spectra show enhanced absorption in Zn-SSZ-13, which can be attributed to the strong electronic interactions between Zn species and lattice

oxygen (O_2^-) in the Si-O-Zn structure (Figure S3) [30]. N_2 adsorption-desorption analysis reveals that Zn incorporation increases the surface area and micropore volume of SSZ-13, while slightly decreasing the average pore size, indicating a framework distortion that generates a more confined yet accessible pore environment. Subsequent Cu exchange leads to a reduction in both surface area and pore volume, confirming that Cu species are preferentially accommodated within the zeolite cages. (Figure S4, S5 and Table S1) [31–33].

Given the critical role of Cu species in methane activation, understanding their local coordination environment and electronic structure is essential for revealing the origin of the Zn promotion effect. Figure 2a shows the Cu k-edge X-ray absorption near edge structure (XANES) spectra of Cu/SSZ-13 and Cu/Zn-SSZ-13 after treatment under different atmospheres. The weak pre-edge peak around 8977 eV is typically assigned to the *1s→3d* transition of Cu^{2+} [34–35], while the pronounced characteristic peak at 8981 eV is assigned to the dipole allowed *1s→4p* transition of Cu^+ [36–39]. The coexistence and interconversion of Cu^{2+} and Cu^+ species further support the involvement of a Cu^{2+}/Cu^+ redox couple during methane oxidation, as proposed previously [40–42]. Notably, compared with Cu/SSZ-13, Cu/Zn-SSZ-13 exhibits a more pronounced Cu^+ feature and a slight shift of the absorption edge toward higher energy, implying that Zn facilitates a more efficient redox process, likely accompanied by partial electron transfer from Cu to the Zn modified framework.

The corresponding EXAFS spectra are shown in Fig. 2b, with fitting results summarized in Table S2. For the N_2-treated Cu/Zn-SSZ-13, the spectrum is dominated by the first shell Cu-O scattering at 1.92 Å [43]. Upon the reaction gas atmosphere, the Cu-O coordination number slightly decreases to 3.2 at 1.93 Å, while a Cu-Cu scattering path emerges, consistent with partial reduction of Cu^{2+} to Cu^+ [42, 44]. Crucially, compared with Cu/SSZ-13, the Cu-Cu coordination number in Cu/Zn-SSZ-13 increased from 0.78 to 0.88, while the Cu-Cu bond length increased from 2.85 to 2.93 Å. This longer Cu-Cu distance (2.93 Å) deviates from the typical Cu_2O_2 dimers but perfectly matches higher nuclearity Cu_xO_y clusters, such as trinuclear Cu_3O_3 clusters confined within zeolite cages. These results suggest that framework Zn modifies the local coordination environment and promotes the formation of multinuclear Cu_xO_y species [45–47].

In the wavelet transform (WT) contour plots of the EXAFS signals (Figs. 2c-e), the maximum intensity at lower k values reflects backscattering from lighter coordinating oxygen atoms (Cu-O path), whereas the high k maximum originates from backscattering of heavier neighboring copper atoms (Cu-Cu path). A comparison of these three contour plots reveals that the introduction of Zn and the varied treatment conditions significantly alter the energy distribution and the maximum intensity position of the signals in the high k region. This provides precise spectroscopic evidence confirming the formation of Cu_3O_3 clusters with specific nuclearities. To further understand how framework Zn influences the location, stability, and evolution of these multinuclear Cu_xO_y species, DFT calculations were performed by considering the distinct Cu hosting sites within the CHA framework. The CHA framework of SSZ-13 consists of double six membered rings (6R) and ellipsoidal large cages connected by eight membered

ring (8R) windows. To balance the negative lattice charge, copper cations preferentially occupy these substructures, such as the 6R sites and positions near the 8R windows. To further identify the nature of Cu species confined in the 6R and 8R cages, DFT calculations were performed to construct T-P(O_2) phase diagrams for Cu/SSZ-13 and Cu/Zn-SSZ-13 (Figure S6) [7, 47]. Considering all plausible Cu_xO_y configurations reported in Cu zeolites (CuO, Cu_2O, CuO_2, Cu_2O_2, and Cu_3O_3), the most stable structures in the 6R and 8R were identified via DFT calculations. For Cu/SSZ-13, Cu_2O_2 and Cu_2O dominate in the 6R, whereas Cu_2O_2 and Cu_3O_3 are favored in the 8R (Figure S7). After Zn incorporation, however, the accessible phase space expands, with Cu_2O, Cu_2O_2, and Cu_3O_3 becoming competitive in the 6R (Fig. 2f), while Cu_3O_3 and Cu_2O dominate in the 8R (Fig. 2g). Moreover, Cu_2O_2 is more stable than Cu_3O_3 by 0.59 eV in Cu/SSZ-13, whereas Cu_3O_3 becomes more stable than Cu_2O_2 by 0.20 eV in Cu/Zn-SSZ-13. This shift indicates that framework Zn alters the relative stability of Cu_xO_y species, favoring higher-nuclearity configurations. Under mild oxygen activation conditions (500 °C, 1 atm), both catalysts favor Cu_2O_2 in the 6R (Fig. 2h). In contrast, within the 8R cages, Cu/SSZ-13 remains dominated by Cu_2O_2, whereas Cu/Zn-SSZ-13 preferentially stabilizes Cu_3O_3 (Fig. 2i). The average Cu-O and Cu-Cu bond lengths for Cu_2O_2 in the 6R of Cu/Zn-SSZ-13 are 1.93 and 2.57 Å, respectively, while the corresponding values in the 8R are 1.85 Å and 3.02 Å (Table S3), in excellent agreement with the EXAFS results. Together, spectroscopic characterization and DFT analysis demonstrate that framework-incorporated Zn induces a reconfiguration of Cu_xO_y ensembles, promoting the stabilization of Cu_2O_2 in the 6R and, critically, Cu_3O_3 in the expanded 8R cages of Cu/Zn-SSZ-13 after oxygen activation.

To correlate the Zn induced structural modulation of Cu species with catalytic performance, the catalysts were evaluated under identical reaction conditions (Fig. 3a, Table S4). Control experiments reveal that neither pristine SSZ-13 nor Zn-SSZ-13 produce detectable methanol, unambiguously confirming that framework Zn species are intrinsically inactive for methane oxidation. The introduction of Cu is essential for the activity, with the baseline Cu/SSZ-13 catalyst delivering a methanol yield of 303.1 μmol g^{-1} h^{-1}. Notably, co-incorporating Zn dramatically boosts this performance, indicating that Zn serves as a critical structural promoter for the Cu active sites. To disentangle the driving forces behind the superior activity of Cu/Zn-SSZ-13, its performance was further investigated under different operational modes (Fig. 3b). A purely photocatalytic pathway can be excluded, as no detectable methanol is produced under irradiation in the absence of external heating. While thermal catalysis alone achieves a substantial yield of 408.1 μmol g^{-1} h^{-1}, introducing light irradiation under thermal conditions further enhances the yield to a maximum of 466.8 μmol g^{-1} h^{-1}. This 14.4% enhancement over its own thermal performance demonstrates that framework Zn does not act as a direct active site. Instead, it reshapes the zeolite microenvironment to promote the formation of highly active Cu species and uniquely unlocks their capacity for photothermal synergistic activation.

The effects of reaction conditions, including gas ratios and catalyst structure, were systematically investigated to ensure optimal catalytic performance (Figures S8-S14). XRD and XPS patterns of catalysts with different structures, as well as those after the reaction, indicate that the catalyst structure

remains intact (Figure S15, S16, S17). A 100-h stability test further demonstrates the robustness of Cu/Zn-SSZ-13, with no appreciable loss in activity or selectivity (Fig. 3c). Compared with previously reported Cu based zeolites, Cu/Zn-SSZ-13 delivers a substantially higher methanol yield (466.8 μmol g^{-1} h^{-1} versus 3.1-280.6 μmol g^{-1} h^{-1}), while maintaining competitive selectivity (Table S5 and Fig. 3d). Furthermore, the catalyst retains good catalytic activity even under low methane concentrations (Figure S18), indicating its applicability under diluted conditions.

To gain deeper insights into the intrinsic driving mechanism behind the photothermal synergistic effect, macroscopic reaction kinetics were systematically investigated. Figure 3e displays the Arrhenius plots, illustrating the relationship between the natural logarithm of the reaction rate constant and the reciprocal of temperature for the various catalytic systems. All plots exhibit excellent linearity, indicating that the reactions follow classical Arrhenius behavior [48]. The slopes of these linear fits directly correlate with the magnitude of the reaction energy barriers. The apparent activation energies quantitatively extracted from the Arrhenius equation are compared in Fig. 3f. The unmodified benchmark catalyst, Cu/SSZ-13, exhibits a high E_a of 32.59 kJ mol^{-1}. Upon the incorporation of framework Zn heteroatoms, the E_a substantially decreases to 29.02 kJ mol^{-1}. This reduction implies that Zn doping thermodynamically optimizes the intrinsic electronic structure of the active sites, effectively lowering the energy barrier for the rate determining step. Most remarkably, when the Cu/Zn-SSZ-13 catalyst is subjected to light irradiation, the E_a undergoes a further distinct drop to a minimum of 28.11 kJ mol^{-1}. This stepwise reduction in activation energy provides compelling kinetic evidence that a strong synergistic effect exists between photon irradiation and the Zn modulated Cu active sites, successfully circumventing the kinetic limitations of purely thermal driven pathways.

The photophysical properties of the catalysts further support this synergistic interaction. UV-vis diffuse reflectance spectra shows that Cu/Zn-SSZ-13 exhibits markedly stronger absorption than either Cu/SSZ-13 or Zn-SSZ-13 (Figure S3), reflecting enhanced light harvesting capability. In addition, Cu/Zn-SSZ-13 displays significantly suppressed photoluminescence intensity and a much smaller electrochemical impedance spectroscopy (EIS) Nyquist arc radius (Figure S19, S20), indicating more efficient charge separation and faster interfacial charge transfer [49–51]. These features collectively rationalize why light irradiation enhances methane conversion only in the Cu/Zn system.

To gain mechanistic insight into the origin of the Zn induced promotion effect, the electronic interaction between framework Zn and confined Cu species was investigated by electron paramagnetic resonance (EPR) spectroscopy. EPR spectra reveals the emergence of unsaturated Zn^{d+} species ($0 < d < 2$) exclusively in Cu/Zn-SSZ-13 (Fig. 4a), providing direct evidence for Cu-Zn electronic coupling [18, 51], which is consistent with the XANES results. EPR spectroscopy under different atmospheres was used to monitor the structural evolution and reversibility of the active centers while the catalyst was sequentially exposed to N_2, CH_4, and O_2 at elevated temperatures (Fig. 4b). In the initial N_2 purging state (gray curve), the sample shows a low peak intensity, consistent with the presence of multinuclear copper-oxo clusters (Cu_2O_2 and Cu_3O_3). When CH_4 was introduced (red curve), the EPR signal intensity significantly

increased. This phenomenon indicates that methane molecules cleave the bridge oxygen bonds within the originally antiferromagnetically coupled copper-oxo clusters. This structural cleavage liberates magnetically isolated Cu^{2+} species while simultaneously inducing a partial reduction of the copper center, generating a transient $Cu^{(2-\delta)}$ ($0 < \delta < 1$) intermediate state. After switching from CH_4 to O_2 (blue curve), the EPR decreased, suggesting that oxygen molecules convert Cu^{+} (or Cu^{2+} intermediates) back into Cu_2O_2 and Cu_3O_3 clusters. The O_2 curve intensity lies between the CH_4 and N_2 baselines, revealing a redox cycle of Cu^{2+}/Cu^{+} during the reaction. The synchronous variation in the paramagnetic intensities of Zn^{d+} and Cu^{2+} confirms that Zn acts as an electronic promoter, regulating the structural evolution of Cu sites and the methane activation process through charge transfer with Cu species. These EPR observations imply a dynamic electronic communication between Cu and framework Zn during the catalytic cycle.

To gain further insight into the associated charge redistribution, XPS analysis was performed to examine the electronic states of Cu and framework Zn species. The Cu 2p spectrum of Cu/SSZ-13 after O_2 activation exhibits a dominant peak at 936.0 eV, characteristic of Cu^{2+} (Fig. 4c) [52]. In Zn-SSZ-13, the Zn $2p_{3/2}$ region shows two contributions at 1021.6 and 1024.6 eV, assigned to ZnO aggregates and framework $ZnOH^{+}$ species (Fig. 4d) [53–54], respectively. Upon co-incorporation of Cu and Zn, the Cu 2p binding energy shifts positively by ~ 0.3 eV, whereas the Zn 2p binding energy shifts negatively by ~ 0.4 eV, evidencing electron transfer from Cu to Zn (Fig. 4e). Bader charge (Table S6) and charge density difference analysis (Figure S21) revealed that in Cu/SSZ-13 and Zn-SSZ-13, Cu (Δq = 1.04 |e|) and Zn (Δq = 1.43 |e|) donated electrons to the zeolite framework. Correspondingly, the metal sites appeared blue (electron depletion) and the framework sites yellow (electron accumulation) in the charge density difference maps. In Cu/Zn-SSZ-13, the electron loss of Cu slightly increased (Δq = 1.10 |e|), while that of Zn slightly decreased (Δq = 1.31 |e|). Meanwhile, an overlapping yellow electron cloud appeared between Cu and Zn, indicating electron transfer from Cu to Zn and the formation of a synergistic effect.

The introduction of Zn into the framework directly altered the surface acidity distribution of the zeolite and enhanced its adsorption capacity for methane (Figure S22, S23, Table S7), thereby exerting a direct influence on the reaction mechanism. The reaction mechanism of direct oxidative methane methylation over Cu/Zn-SSZ-13 was investigated by EPR and diffuse reflectance infrared Fourier transform spectroscopy (DRIFTS) measurements under reaction conditions.

In the spin trapping EPR spectra, the characteristic 1:2:2:1 quartet signal is assigned to DMPO-•OH adducts (Fig. 5a), whereas the six line splitting pattern with four intense and two weaker peaks corresponds to DMPO-•O_2^- adducts (Fig. 5b) [48, 55–56]. No radical signals are detected for any catalyst in the dark. Cu/SSZ-13 shows no DMPO-•OH or DMPO-•O_2^- signals even under irradiation, consistent with its negligible photo response. In contrast, both Zn-SSZ-13 and Cu/Zn-SSZ-13 generate detectable radical species, with Cu/Zn-SSZ-13 exhibiting substantially higher signal intensities. This result indicates that Cu-Zn synergy significantly enhances the formation of reactive oxygen species, which is attributed to

improved charge separation and more efficient O_2 activation. Moreover, Zn incorporation markedly increases the intensity of the DMPO-•CH_3 adduct signal (Fig. 5c), demonstrating a higher concentration of •CH_3 intermediates and confirming that framework Zn promotes C-H bond cleavage in methane [55]. Collectively, framework Zn functions as an efficient light harvesting and charge modulating center that enhances light absorption, charge separation, and interfacial charge transfer, thereby facilitating the generation of key reactive intermediates (•OH, •O_2^-, and •CH_3) under photothermal conditions.

The evolution of surface species was further monitored by in situ DRIFTS. The bands at 1305 and 3014 cm^{-1} are assigned to the bending and antisymmetric stretching vibrations of adsorbed methane (Figure S24) [57]. The absorption at 902 cm^{-1} corresponds to Cu^{2+} species (Fig. 5d) [8], while a new band at 2153 cm^{-1} [58–59], characteristic of Cu^+, emerges upon reaction. As the reaction proceeds, the 902 cm^{-1} band gradually diminishes, whereas the 2153 cm^{-1} band increases and eventually reaches a steady state, confirming the dynamic conversion of Cu^{2+} to Cu^+ during methane oxidation.

DFT calculations further clarify the structure activity relationship. For Cu/SSZ-13, the energy barriers for CH_3OH formation are 0.34 eV on 6R Cu_2O_2 sites and 1.60 eV on 8R Cu_2O_2 sites (Fig. 5e), indicating that methane conversion preferentially occurs in 6R cages [8]. In Cu/Zn-SSZ-13, however, the barriers are substantially reduced to 0.21 eV on Cu_2O_2 and 0.04 eV on Cu_3O_3 sites (Fig. 5f), explaining the markedly enhanced activity. The Cu 3d band centers shift from − 2.55 eV (6R) and − 2.34 eV (8R) in Cu/SSZ-13 to -2.62 eV and − 2.59 eV, respectively, after Zn incorporation (Figure S25), indicating weakened Cu-CH_4 interactions and facilitated C-H activation [60–61]. Methanol desorption was also examined computationally. On Cu_2O_2 and Cu_3O_3 clusters in Cu/Zn-SSZ-13, the CH_3OH desorption energies are 0.40 and 0.44 eV at 425 ℃, suggesting sluggish desorption under dry conditions. Upon co-adsorption of H_2O, these values decrease dramatically to 0.02 and − 0.01 eV, indicating facile methanol release. This prediction is fully consistent with catalytic performance [62].

For Cu/SSZ-13, methane activation occurs on confined Cu_2O_2 species via a thermally driven Cu^{2+}/Cu^+ redox cycle. CH_4 adsorption and C-H bond cleavage generates surface bound *CH_3 intermediates, which are subsequently oxidized to *CH_3OH. Under light irradiation, neither the electronic structure nor the configuration of Cu_xO_y species is appreciably altered, leading to nearly identical activities under thermal and photothermal conditions. In Cu/Zn-SSZ-13, the introduction of framework Zn introduces an additional light responsive pathway that does not directly activate methane. Upon irradiation, Zn centered electronic states promote charge redistribution within the zeolite cages, strengthening the interaction between neighboring Cu species and driving the reorganization of confined Cu_xO_y ensembles. During O_2 activation, this process shifts the dominant copper motifs from Cu_2O_2 toward higher nuclearity Cu_3O_3 clusters, particularly in the expanded 8R cages. These reconfigured sites more efficiently stabilize *CH_3 intermediates and lower the energetic barrier for C-H bond cleavage.

Conclusion

In summary, this study demonstrates that framework incorporated Zn in SSZ-13 zeolites enables a continuous photothermal catalytic pathway for the DOMM by modulating the structure and electronic properties of confined Cu_xO_y active sites. Under optimized conditions, Cu/Zn-SSZ-13 achieves a methanol yield of 466.8 μmol g^{-1} h^{-1} with 79.1% selectivity and maintains stable performance over 100 h, representing a substantial improvement over conventional Cu/SSZ-13 operating under purely thermal conditions. Further mechanistic insights show that Cu species are confined within the CHA cages as Cu_2O_2 and Cu_3O_3 clusters following O_2 activation, with framework Zn inducing interfacial charge transfer that preferentially stabilizes larger Cu_3O_3 motifs. Rather than directly initiating methane activation, light acts to regulate thermal catalysis by subtly reshaping the electronic structure and population of Cu_xO_y species through Zn mediated electronic modulation. During this process, O_2 serves as the sole oxidant. Taken together, these findings establish a framework enabled photothermal strategy that enables active site modulation without direct participation of the secondary element in methane activation, offering a broadly applicable approach for the rational design of selective methane conversion catalysts.

Methods

Materials and Chemicals. All chemicals were used as purchased without further purification. Tetraethyl orthosilicate (TEOS, 99%), zinc acetate anhydrous [$(CH_3COO)_2Zn$, 99.5%], aluminum isopropoxide (AIP, 99.8%), Ammonia solution ($NH_3{\cdot}H_2O$, 25–28%), was purchased from Shanghai Macklin Biochemical Co., Ltd. N,N,N-trimethyl-1-adamantylammonium hydroxide (TMAdaOH, 25% aqueous solution), Copper(Ⅱ) acetate monohydrate[$(CH_3COO)_2Cu$, 99%], Hydrofluoric acid (HF, ACS) was purchased from Shanghai Aladdin Biochemical Technology Co., Ltd. CH4 (99.999%), O_2 (99.999%), N_2 (99.999%) was purchased from Taiyuan Taineng Gas Co., Ltd.

Catalyst preparation.

Zn-SSZ-13 zeolite was synthesized via a hydrothermal method using tetraethyl orthosilicate (TEOS, SiO_2 source), zinc acetate anhydrous [$(CH_3COO)_2Zn$, Zn source], aluminum isopropoxide (AIP, Al source), and N,N,N-trimethyl-1-adamantylammonium hydroxide (TMAdaOH, structure-directing agent). The molar composition of the gel was optimized as: TEOS/$(CH_3COO)_2Zn$/AIP/TMAdaOH/H_2O/HF = 1/x/y/0.5/3/0.5, where x = 0.008, 0.016, 0.024 and y = 0.10, 0.067, 0.054, 0.050. For example, when x = 0.016 and y = 0.054, 4.095 mL of TMAdaOH was mixed with 0.11 g of AIP and sonicated homogeneously and recorded as solution A. TEOS was mixed with $(CH_3COO)_2Zn$ and recorded as mixture B. Subsequently, mixture B was added slowly dropwise to solution A under vigorous stirring, and a homogeneous and clarified solution was obtained after stirring for 5 h and recorded as solution C. The solution A was then mixed with $(CH_3COO)_2Zn$ and stirred well. Solution C was heated at 60 ℃ for 3 h, TEOS/H_2O = 1/3 was adjusted, and 0.234 ml of HF was added to obtain a white gel, which was stirred well. The gel was transferred to a Teflon lined stainless steel autoclave and heated at 170 ℃ for 48 h.

After crystallization was complete, the product was washed with deionized water, dried at 110 ℃ for 12 h, and calcined at 600 ℃ for 6 h (ramp rate: 1 ℃/min).

The Cu/Zn-SSZ-13 catalyst was synthesized using an ion exchange method. In a typical procedure, 1 g of Zn-SSZ-13 was dispersed in 50 mL of copper acetate [$(CH_3COO)_2Cu$] aqueous solution with varying concentrations (0, 0.005, 0.008, 0.01 M) and stirred in a constant temperature water bath at 25 ℃ for 8 h under light conditions. The pH was maintained at 5.5 by dropwise addition of 1 M $NH_3{\cdot}H_2O$. The solid product was filtered, washed three times with deionized water, and dried at 110 ℃ for 12 h. The ion exchange process was repeated three times to ensure complete Cu loading. The final product was calcined at 600 ℃ for 6 h in air with a heating rate of 1 ℃ min^{-1}. Cu/SSZ-13 was prepared under identical conditions using pristine SSZ-13 (without Zn doping) and 0.008 M $(CH_3COO)_2Cu$ solution.

Characterizations. Powder XRD patterns were recorded on a MiniFlexII diffractometer using Cu-Kα radiation (λ = 1.5418 Å, 40 kV, 40 mA) over a 2θ range of 5–50°. FTIR spectra were collected on a Bruker TENSOR27 spectrophotometer using KBr pellets in the 400–4000 cm^{-1} range. N_2 adsorption-desorption isotherms at -196 ℃ were measured on a Micromeritics ASAP 2020 PLUS HD88 analyzer. The specific surface area was calculated using the Brunauer-Emmett-Teller (BET) method. Morphology was analyzed using a Hitachi SU8010 SEM equipped with an energy dispersive X-ray spectroscopy (EDS) detector. UV-Vis DRS was performed on a PerkinElmer LAMBDA 650 spectrophotometer using $BaSO_4$ as a reference, covering 200–800 nm. Elemental composition was determined using Avio 500 ICP-OES. Acidic properties were analyzed by NH_3-TPD on a ChemiSorb 2720 system. EPR spectra were recorded on a Bruker Elexsys A300 spectrometer to detect radical species ($\bullet CH_3$, $\bullet OH$, $\bullet O_2^-$). PL spectra were collected on an FLS980 spectrofluorometer with an excitation wavelength of 250 nm. EIS measurements were conducted on a Princeton Applied Research PMC 1000 workstation using a three electrode system: Ag/AgCl (reference), Pt foil (counter), and catalyst coated glassy carbon (working electrode). In situ DRIFTS was performed on a Nicolet IS50 FTIR spectrometer. Samples were pretreated under N_2 flow at 250 ℃ for 20 min, followed by exposure to a $CH_4/O_2/H_2O$ mixture. Spectra were collected at 0, 1, 5, 10, and 20 min intervals. Illumination dependent spectra were acquired under Xe lamp irradiation. CH_4 adsorption capacity was evaluated via CH_4-TPD: 50 mg catalyst was heated to 550 ℃ at 10 ℃ min^{-1}under He flow (30 mL min^{-1}) for 1 h. After cooling to 45 ℃, the sample was exposed to 50% CH_4/He (30 mL min^{-1}) for 1 h. He flows (30 mL min^{-1}) at 45 ℃ for 30 min. Temperature ramped from 45 ℃ to 600 ℃ at 10 ℃ min^{-1} under He flow. Electron spin resonance (EPR) spectrawere recorded using a JEOL JES FA200 spectrometer at 9.8 GHz, X-band, with 100 Hz field modulation. For the detection of Zn^{d+} and Cu^{2+}, the detector temperature was 77 K. Characterisation of the coordination environment of catalysts using synchrotron radiation. Cu K-edge XAFS analyses were performed with Si (111) crystal monochromators at the BL14W Beam line at the Shanghai Synchrotron Radiation Facility (SSRF) (Shanghai, China). Before the analysis at the beamline, samples were placed into aluminum sample holders and sealed using Kapton tape film. The XAFS spectra were recorded at room temperature using a 4 channel Silicon Drift Detector (SDD) Bruker 5040. Cu K-edge extended X-ray

absorption fine structure (EXAFS) spectra were recorded in transmission/fluorescence mode. Negligible changes in the line shape and peak position of Cu K-edge XANES spectra were observed between two scans taken for a specific sample. The EXAFS spectra of these standard samples were recorded in transmission mode. The spectra were processed and analyzed by the software codes Athena. Additional characterizations not described above were used to further clarify the framework incorporation of Zn, the dispersion state of Cu species, and the electronic interaction between Cu and Zn. Solid state ^{29}Si MAS NMR spectroscopy was employed to probe the local coordination environment of Si atoms and to verify the formation of Si-O-Zn linkages, thereby confirming that Zn species were incorporated into the zeolite framework rather than existing only as extra framework species. HAADF-STEM and elemental mapping were used to observe the morphology, elemental distribution, and dispersion state of Cu and Zn species in the zeolite crystals. The high angle annular dark-field contrast provided direct evidence for the presence of confined Cu containing clusters. X-ray photoelectron spectroscopy (XPS) was performed to analyze the surface chemical states of Cu and Zn species and to evaluate the electronic interaction between confined Cu species and framework Zn sites. The shifts in Cu 2p and Zn 2p binding energies were used as indicators of interfacial charge transfer between Cu and Zn species.

Activity evaluation Methane oxidation to methanol with O_2 by photocatalysis, thermal catalysis, and photothermal catalysis was carried out in a fixed bed reactor at ambient pressure. The fixed bed reactor featured a hole in the furnace wall and utilized a quartz tube (6 mm inner diameter) to allow illumination from a Xe lamp (CEL-HXFUV300T3, 200–400 nm, 360 mW cm^{-2}). Typically, 0.1 g catalyst (250–425 μm) was placed in the quartz reactor. Initially, the catalyst was activated at 500 ℃ for 2 h under flowing O_2 and continuous light conditions. Afterward, light and O_2 were maintained while CH_4 and H_2O were fed to the quartz reactor as it cooled to the reaction temperature. The flow rates of the reaction gases were controlled by the independent mass flowmeters. The volume of water vapor was converted to the volume of liquid water, and the liquid water flow rate was controlled by an ultramicro pump. Before entering the reactor, the reaction gas and water were heated by a 320 ℃ heating belt in the respective gas and liquid lines, then mixed and further heated in a 320 ℃ preheater. All heating equipment was temperature controlled by thermocouples. The outlet gas was divided into gas phase and liquid phase products through a condenser. The liquid and gas phase products were collected at one hour intervals and analyzed by a gas chromatograph (Agilent 7890B) equipped with a methanizer, a flame ionization detector (FID, with one DBWAX column) and a thermal conductivity detector (TCD, with one TDX-01 packed column). 1H NMR was performed on a Bruker AVANCE NEO (600 MHz) spectrometer to identify the type of liquid product. The yield of liquid phase product L (Y_L) was calculated as follows:

$$Y_L = \frac{C * \nu}{M{*}\mathrm{m}{*}\mathrm{t}}$$

Where Y_L is the yield of L (μmol g^{-1} h^{-1}), c is the mass concentration of L (mg L^{-1}), v is the volume of outlet liquid phase (mL), M is the molar mass of CH_3OH (g mol^{-1}), m is the amount of catalyst, and t is the reaction time (h).

The yield of gas phase product G (Y_G) was calculated as follows:

$$Y_G = \frac{\chi * \mathrm{p}^* V}{R * T * \mathrm{m}^* \mathrm{t}}$$

Where Y_G is the yield of G (mmol mol_{Cu}^{-1} h^{-1}), x is the volume fraction of G, p is the ambient pressure (Pa), V is the volume of outlet gas phase (m^3), R is the molar gas constant (J mol^{-1} K^{-1}), and T is the ambient temperature (K).

The selectivity of CH_3OH (S_{CH3OH}) was obtained as follows:

$$S_{CH3OH} = \frac{Y_{CH3OH}}{\Sigma\, Product}$$

DFT calculations

Density functional theory (DFT) was performed using the Vienna Ab Initio Simulation Package [63–65]. The generalized gradient approximation (GGA) with the PBE functional and pseudopotential generated in the projector-augmented wave method were employed [66]. A 2 × 2 × 3 Monkhorst-Pack k-point grid was used for sampling the first Brillouin zone of the above model. A cutoff energy of 415 eV was sufficient to obtain a satisfactory convergence of the total energy. The climbing image nudged elastic band (CI-NEB) method was utilized to locate transition states (TS).

SSZ-13 was a material with the chabazite structure, the zeolite framework structure with the smallest primitive unit cell. $Si_{48}O_{96}$ model was used (Figure S8a). The framework was composed of corner sharing SiO_4 tetrahedral (T-sites), which formed a double six O-ring (6R) building block; The unit cells were connected by four O-rings, which leaded to a medium sized pore and the formation of eight O-rings (8R). ICP result shown that the atomic ratio of Zn: Si :Al with the highest methanol yield was 2.34 : 96 : 6. Therefore, $ZnAl_3Si_{44}O_{96}$ was used (Figure S8b), which was in accordance with our ICP results.

The ΔG of the Cu_xO_y cluster in the SSZ-13 was defined as:

$\Delta G(Cu_xO_y\text{-SSZ-13}) = G(Cu_xO_y\text{-SSZ-13}) - xG(\text{Cu-SSZ-13}) - 0.5yG(O_2)$

where $G(Cu_xO_y\text{-SSZ-13})$, G(Cu-SSZ-13) and $G(O_2)$ are the Gibbs free energies of Cu_xO_y-SSZ-13, Cu-SSZ-13 and O_2 molecules, respectively. For the condensed phases, we can neglect the entropic and *p*V terms, as well as thermal variations of internal energies. Therefore, ΔG is equal to the equation:

$\Delta G(Cu_xO_y\text{-SSZ-13}) = E(Cu_xO_y\text{-SSZ-13}) - E(\text{Cu-SSZ-13}) - 0.5y\ \mu(O_2)$

In this equation, $\mu(O_2)$ is the chemical potential of O_2 molecules. The chemical potentials of O_2 molecule depends on temperature and pressure according to [67–69]

$\mu(O_2)(T, p) = E(O_2) + \tilde{\mu}(O_2)(T, p^0) + k_B T \ln[p(O_2)/p^0]$

where p^0 represents the standard atmospheric pressure, $\tilde{\mu}(O_2)$ is the chemical potential of oxygen gas at 1 atm, including the contribution from vibration and rotation of O_2 molecules. We used the experimental values from thermodynamic tables [70].

Data availability

The data that support the findings of this study are available in the Supporting Information of this article.

Declarations

Acknowledgments

The authors would like to thank the National Natural Science Foundation of China (No. U25A20554, 22322815, 22179146 and 22138013), State Key Laboratory of Coal Liquification, Gasification and Utilization with High Efficiency and Low Carbon Technology (Open Fund Project No.SKL/SE-OF-202504), Central Government Guides the Local Science and Technology Development Special Fund (YDZJSX2024D027), Shandong Provincial Natural Science Foundation (Grant No. ZR2025QA14) for their financial.

Author Contributions

Z.Z. conceived and supervised the project. L.L. and W.W. co- supervised the project. J.H., and H.Z. conducted most experiments including synthesis, characterization and testing, as well as data analysis. Y.Z. carried out DFT calculations section. C.S. performed characterization and testing analysis. Y.S. conducted spectrum analysis. Q.S. provided advice and expertise. J.H., H.Z., and Z.Z. wrote and revised the paper. All authors discussed the paper.

Competing interests

The authors declare no competing interests.

References

1. Zuo Z et al (2016) Low-Temperature Conversion of Methane to Methanol on CeO_x/Cu_2O Catalysts: Water Controlled Activation of the C-H Bond. J Am Chem Soc 138:13810–13813
2. Wang WJ et al (2025) Continuous Selective Oxidation of Methane To Methanol by Thermal-Assisted Photocatalysis over NiO/ZnO. J Colloid Interface Sci 699:138190
3. Shah MSAS et al (2020) Catalytic Oxidation of Methane to Oxygenated Products: Recent Advancements and Prospects for Electrocatalytic and Photocatalytic Conversion at Low

Temperatures. Adv Sci 7:2001946

4. Lv H et al (2024) Plasma-Catalytic Direct Oxidation of Methane To Methanol over Cu-MOR: Revealing the Zeolite-Confined Cu^{2+} Active Sites. Chem Eng J 496:154337
5. Yan Z et al (2026) Synergy between Brønsted Acid Sites and Cu/Zn Single-Atom Sites in Zeolite for the Direct Oxidation of Methane. J Am Chem Soc 148:17753–17763
6. Xiao P et al (2024) Revealing Active Sites and Reaction Pathways in Direct Oxidation of Methane over Fe-Containing CHA Zeolites Affected by the Al Arrangement. J Am Chem Soc 146:31969–31981
7. Brenig A et al (2025) Tracking Active Site Formation during Oxidative Activation of Copper-Exchanged Zeolites for Methane-to-Methanol Conversion. Adv Sci 12:2413870
8. Zhang H et al (2023) Confined Cu-OH Single Sites in SSZ-13 Zeolite for the Direct Oxidation of Methane To Methanol. Nat Commun 14:7705
9. Rebolledo-Oyarce J et al (2025) Heterogeneous and Framework-Bound Copper Species Contribute to Catalytic Partial Methane Oxidation in Cu-Chabazite Zeolites. ACS Catal 15:10198–10209
10. Kilburn L et al (2026) Quantification of Cu Site Contributions to Partial and Overoxidation Reactions of Methane during Stoichiometric Cycles on Cu-CHA Zeolites. J Catal 453:116507
11. Zhou X et al (2021) One-Pot Hydrothermal Synthesis of Dual Metal Incorporated CuCe-SAPO-34 Zeolite for Enhancing Ammonia Selective Catalytic Reduction. J Hazard Mater 405:124177
12. Oda A et al (2025) Hydrophobic, Acid-Free Zeolite-Confined Pt-Cu Nanoalloys Break Activity Selectivity Limits in Low-Temperature Methane-to-Methanol Oxidation. J Am Chem Soc 147:30009–30021
13. Wang W et al (2024) Photothermal Catalytic Methane Oxidation to Methanol on Cu/Ti-ZSM-5. *Fuel* 376, 132720
14. Deng Y et al (2023) Transition-Metal-Promoted Cu-SSZ-13 Catalysts for Continuous Selective Oxidation of Methane to Methanol Using Molecular Oxygen. ACS Catal 14:292–298
15. Wang Y et al (2022) New Insight into the Doping Effect of Transition Metals (Fe, Ti, Mn, and Ce) on the Structure and Catalytic Performance of Cu-SSZ-13 Zeolite Catalysts for the NH_3-SCR Reaction. Ind Eng Chem Res 61:15066–15075
16. Imasaka S et al (2019) Synthesis of CHA-type Titanosilicate Zeolites Using Titanium Oxide as Ti Source and Evaluation of their Physicochemical Properties. Microporous Mesoporous Mater 273:243–248
17. Eilertsen EA et al (2012) Single Parameter Synthesis of High Silica CHA Zeolites from Fluoride Media. Microporous Mesoporous Mater 153:94–99
18. Wu W et al (2018) Synergies between Unsaturated Zn/Cu Doping Sites in Carbon Dots Provide New Pathways for Photocatalytic Oxidation. ACS Catal 8:747–753
19. Zhang Y et al (2022) Revealing the Synergistic Deactivation Mechanism of Hydrothermal Aging and SO_2 Poisoning on Cu/SSZ-13 under SCR Condition. Environ Sci Technol 56:1917–1926

20. Lv G et al (2022) Charge Transformation of Framework Titanium (IV) into Titanium (III) in Vanadium-Titanium Doped MFI Zeolite for Enhanced Alkene Epoxidation. Microporous Mesoporous Mater 341:112035
21. Lin H et al (2022) Dealumination-Controlled Strategy Mediates Ti-Y Zeolite with Cooperative Active Sites for Selective Oxidations. Catal Sci Technol 12:4837–4850
22. Li Z et al (2019) Photocatalytic Oxidation of Methane over CuO-decorated ZnO Nanocatalysts. J Mater Chem A 7:469–475
23. Jiang H et al (2019) Cu/SSZ-13 Zeolites Prepared by in situ Hydrothermal Synthesis Method as NH3-SCR Catalysts: Influence of the Si/Al ratio on the Activity and Hydrothermal Properties. Fuel 255:115587
24. Bhadra BN et al (2018) Conversion of Ethylene into Propylene with the Siliceous SSZ-13 Zeolite Prepared without an Organic Structure-Directing Agent. J Catal 365:94–104
25. Su X et al (2023) Biomolecule-Inspired Synthesis of Framework Zinc in MFI Zeolite for Propane Dehydrogenation. Microporous Mesoporous Mater 348:112371
26. Camblor MA et al (1994) Synthesis and Characterization of Zincosilicates with the SOD Topology. Chem Mater 6:2193–2199
27. Guo Y et al (2019) Cost-Effective Synthesis of CHA Zeolites with Controllable Morphology and Size. Chem Eng J 358:331–339
28. Mu Y et al (2017) Effect of Ultrasound Pretreatment on the Hydrothermal Synthesis of SSZ-13 Zeolite. Ultrason Sonochem 38:430–436
29. Zhu Z et al (2025) One-Pot Synthesis of Metal-Containing SSZ-13 Nanocrystals by Interzeolite Transformation of Spent FCC Catalysts for the Methanol-To-Olefins Reaction. Appl Catal B-Environment Energy 365:124900
30. Bing L et al (2024) Bimetallic PtZn Nanoparticles Anchored in High-silica SSZ-13 Zeolite for Efficient Propane Dehydrogenation. Chem Eng J 491:151961
31. Aydani A et al (2021) Silica Sol Gel Assisted Defect Patching of SSZ-13 Zeolite Membranes for CO_2/CH_4 Separation. Sep Purif Technol 277:119518
32. Wang W et al (2019) Preparation of Bifunctional Core-shell Structured Cu/TS-1@MCM-41 Molecular Sieves for Synthesis of Aniline by Benzene in One Step Amination. Microporous Mesoporous Mater 277:163–170
33. Huo JM et al (2024) High-Valence Metal Doping Induced Lattice Expansion for M-FeNi LDH toward Enhanced Urea Oxidation Electrocatalytic Activities. Small 20:230587
34. Imbao J et al (2020) Elucidating the Mechanism of Heterogeneous Wacker Oxidation over Pd-Cu/zeolite Y by Transient XAS. Nat Commun 11:1118
35. Zhang H et al (2024) A Review on the Active Sites for Direct Oxidation of Methane to Methanol by Copper-zeolites: Coordination Structure, Formation and Activity. Coord Chem Rev 503:215637

36. Zhu J et al (2025) Elucidation of the Structure Activity Relationship for Cu-Erionite in the Direct Conversion of Methane to Methanol: An Operando XAS Study. J Am Chem Soc 147:28723–28734
37. Bregante DT et al (2021) Dioxygen Activation Kinetics over Distinct Cu Site Types in Cu-Chabazite Zeolites. ACS Catal 11:11873–11884
38. Kau LS et al (1987) X-ray Absorption Edge Determination of the Oxidation State and Coordination Number of Copper. Application to the Type 3 Site in Rhus Vernicifera Laccase and Its Reaction with Oxygen. J Am Chem Soc 109:6433–6442
39. Sharma A et al (2015) XANES, EXAFS and Photocatalytic Investigations on Copper Oxide Nanoparticles and Nanocomposites. RSC Adv 5:21762–21771
40. Alayon EMC et al (2014) Reaction Conditions of Methane-to-Methanol Conversion Affect the Structure of Active Copper Sites. ACS Catal 4:16–22
41. Martini A et al (2017) Composition-Driven Cu-Speciation and Reducibility in Cu-CHA Zeolite Catalysts: a Multivariate XAS/FTIR Approach to Complexity. Chem Sci 8:6836–6851
42. Ohyama J et al (2022) Relationships among the Catalytic Performance, Redox Activity, and Structure of Cu-CHA Catalysts for the Direct Oxidation of Methane to Methanol Investigated Using In Situ XAFS and UV-Vis Spectroscopies. ACS Catal 12:2454–2462
43. Paolucci C et al (2016) Catalysis in a Cage: Condition-Dependent Speciation and Dynamics of Exchanged Cu Cations in SSZ-13 Zeolites. J Am Chem Soc 138:6028–6048
44. Pappas DK et al (2017) Methane to Methanol: Structure Activity Relationships for Cu-CHA. J Am Chem Soc 139:14961–14975
45. Grundner S et al (2015) Single-Site Trinuclear Copper Oxygen Clusters in Mordenite for Selective Conversion of Methane to Methanol. Nat Commun 6:7546
46. Markovits MAC et al (2016) Effect of Location and Distribution of Al Sites in ZSM-5 on the Formation of Cu-Oxo Clusters Active for Direct Conversion of Methane to Methanol. Top Catal 59:1554–1563
47. Goltl F et al (2024) Exploring the Impact of Active Site Structure on the Conversion of Methane to Methanol in Cu-Exchanged Zeolites. Angew Chem Int Ed 63:e202403179
48. Zhang H et al (2026) FeCu Dual-Single-Atom Catalyst Promotes Gradient H_2O_2 Activation for Enhanced Methane Oxidation to Methanol. Nat Commun 17:3526
49. Duan J et al (2024) Hollow $AMn_2O_{4-\delta}$ (A = Co, Zn, Ni) Nanotube for Direct Photo-Oxidation of Methane to C_1 and C_2 Alcohols at Atmospheric Pressure and Room Temperature. Chem Eng J 485, 149904
50. Liu X et al (2024) Acceleration of the Charge Transfer Rate for Efficient Photocatalytic Hydrogen Production via Adjusting Modulator and Introducing Electronic Bridge Dual Strategies. Fuel 366:131252
51. Nellutla S et al (2005) Magnetism, Electron Paramagnetic Resonance, Electrochemistry, and Mass Spectrometry of the Pentacopper(II)-Substituted Tungstosilicate $[Cu_5(OH)_4(H_2O)_2(A\text{-}\alpha\text{-}SiW_9O_{33})_2]^{10-}$,

A Model Five-Spin Frustrated Cluster. Inorg Chem 44:9795–9806

52. Sainz-Vidal A et al (2014) Preparation of Cu-Mordenite by Ionic Exchange Reaction under Milling: A Favorable Route to Form the mono-(μ-oxo) Dicopper Active Species. Microporous Mesoporous Mater 185:113–120
53. Gabrienko AA et al (2017) Different Efficiency of Zn^{2+} and ZnO Species for Methane Activation on Zn-Modified Zeolite. ACS Catal 7:1818–1830
54. Niu X et al (2017) Influence of Crystal Size on the Catalytic Performance of H-ZSM-5 and Zn/H-ZSM-5 in the Conversion of Methanol to Aromatics. Fuel Process Technol 157:99–107
55. Chen Y-Q et al (2024) An Efficient Au/ZnO Catalyst for the Photocatalytic Conversion of Methane to Formaldehyde. Chem Eng J 498:155792
56. Jiang Y et al (2023) Enabling Specific Photocatalytic Methane Oxidation by Controlling Free Radical Type. J Am Chem Soc 145:2698–2707
57. Yu T et al (2021) Identifying Key Mononuclear Fe Species for Low-Temperature Methane Oxidation. Chem Sci 12:3152–3160
58. Zhou C et al (2022) Temperature-Dependant Active Sites for Methane Continuous Conversion to Methanol over Cu-Zeolite Catalysts Using Water as the Oxidant. Fuel 329:125483
59. Sun L et al (2021) Water-Involved Methane-Selective Catalytic Oxidation by Dioxygen over Copper Zeolites. Chem 7:1557–1568
60. Li D et al (2023) Revealing the Synergistic Mechanism of Generation, Release, Migration and Utilization of Reactive Oxygen Species through Tailoring the d-band in Metal Organic Frameworks for Water Purification. Appl Catal B-Environment Energy 328, 122507
61. Kitchin JR et al (2003) Elucidation of the Active Surface and Origin of the Weak Metal-Hydrogen Bond on Ni/Pt(111) Bimetallic Surfaces: a Surface Science and Density Functional Theory Study. Surf Sci 544:295–308
62. Zhao Z-J et al (2016) Theoretical Insights into the Selective Oxidation of Methane to Methanol in Copper-Exchanged Mordenite. ACS Catal 6:3760–3766
63. Blöchl PE (1994) Projector Augmented-wave Method. Phys Rev B 50:17953–17979
64. Kresse G et al (1996) Efficiency of Ab-initio Total Energy Calculations for Metals and Semiconductors Using a Plane-Wave Basis Set. Comput Mater Sci 6:15–50
65. Kresse G et al (1993) Ab Initio Molecular Dynamics for Liquid Metals. Phys Rev B 47:558–561
66. Perdew JP et al (1996) Generalized Gradient Approximation Made Simple. Phys Rev Lett 77:3865–3868
67. Liu Q et al (2014) Oxygen Chemisorption-Induced Surface Phase Transitions on Cu(110). Surf Sci 627:75–84
68. Shan W (2016) Theoretical Study of Hydrogen-Induced Atomic Evolution of the Oxygen-chemisorbed Cu(110.) Surface

69. Xu Y et al (2001) Adsorption and Dissociation of O_2 on Cu(111): Thermochemistry, Reaction Barrier and The Effect of Strain. Surf Sci 494:131–144
70. Lin L et al (2018) Low-Temperature Hydrogen Production from Water and Methanol using Pt/α-MoC Catalysts. Abstracts Papers Am Chem Soc 255:80–83

Figures

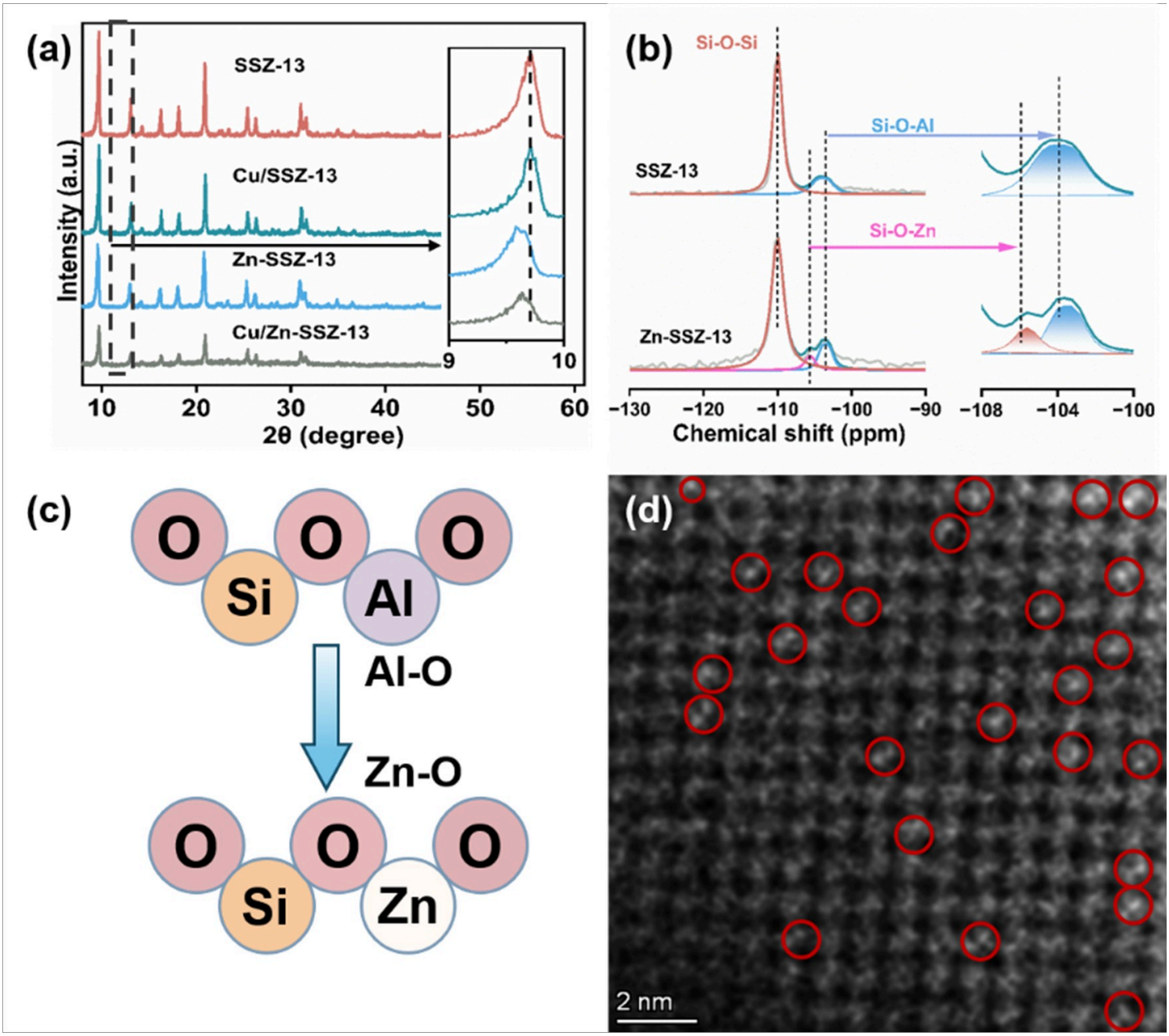


Figure 1

Framework Zn incorporation reconstructs the local environment of confined Cu species. (a) XRD patterns of the synthesized SSZ-13, Cu/SSZ-13, Zn-SSZ-13, and Cu/Zn-SSZ-13. (b) ^{29}Si solid state MAS

NMR spectra of the SSZ-13 and Zn-SSZ-13. (c) Schematic illustration of the isomorphous substitution of Zn into the zeolite framework (forming Si-O-Zn linkages). (d) HAADF-STEM images of Cu/Zn-SSZ-13 (The circled region highlights the Cu-O cluster).

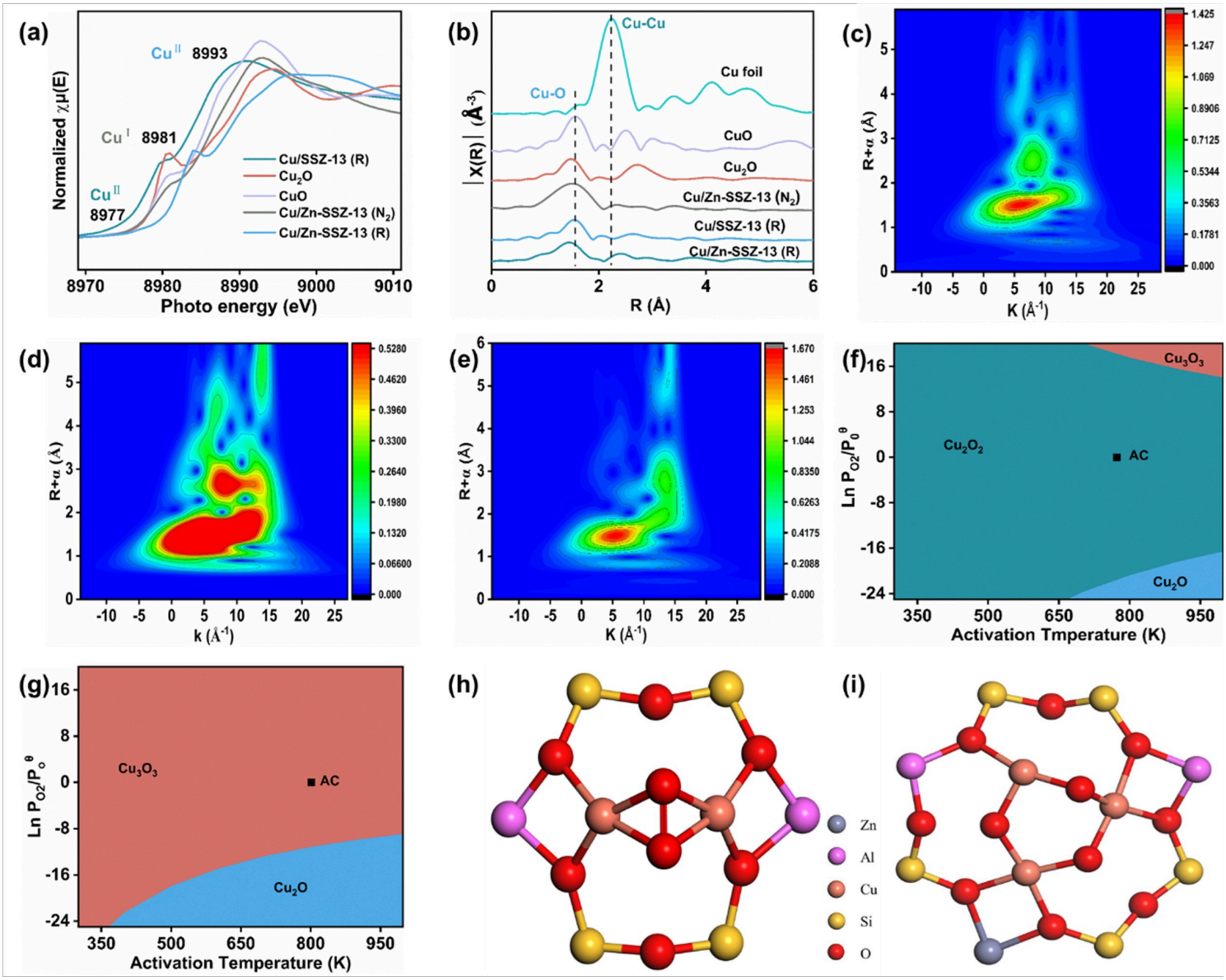


Figure 2

Framework Zn stabilizes larger confined Cu_xO_y clusters. (a) Normalized Cu K-edge X-ray absorption near-edge structure (XANES) spectra of the samples. (b) The corresponding Fourier transform (FT) of the extended X-ray absorption fine structure (EXAFS) spectra in R space. (c-e) Wavelet transform (WT) contour plots of the EXAFS signals for (c) the Cu/Zn-SSZ-13 sample after reaction, (d) the Cu/SSZ-13 sample after reaction, and (e) the Cu/Zn-SSZ-13 sample treated in N_2. (f) Phase diagram of Cu/Zn-SSZ-13-6R, (AC: activation conditions). (g) Phase diagram of Cu/Zn-SSZ-13-8R. (h, i) Diagrams of Cu_xO_y model in Cu/Zn-SSZ-13 6R (h) and 8R (i).

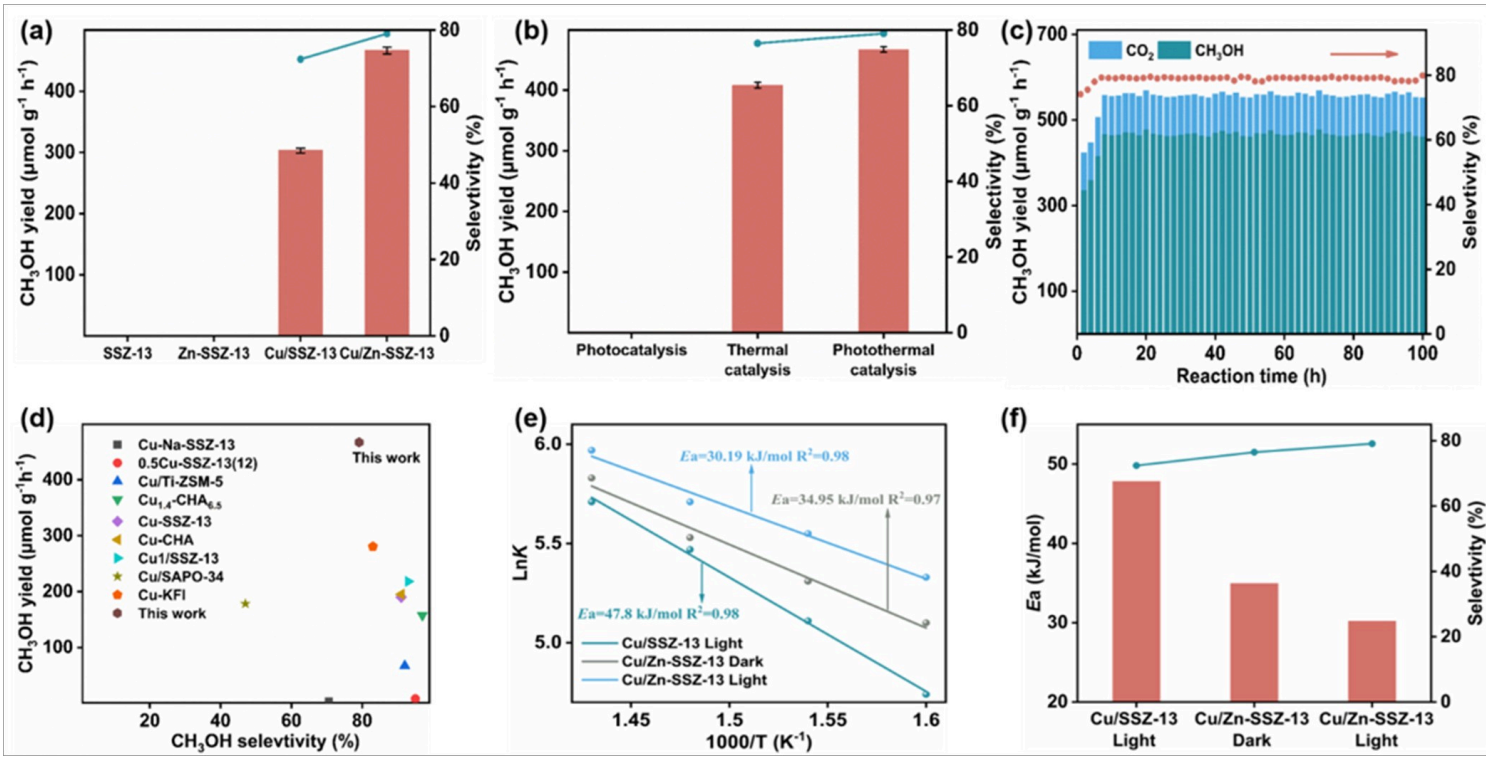


Figure 3

Framework Zn lowers the kinetic barrier for photothermal methane oxidation. (a) Comparison of CH_3OH yield over the SSZ-13, Zn-SSZ-13, Cu/SSZ-13, and Cu/Zn-SSZ-13 catalysts. (b) CH_3OH yield over the Cu/Zn-SSZ-13 catalyst under different reaction modes: photocatalysis, thermal catalysis, and photothermal catalysis. (c) Long term stability test of the Cu/Zn-SSZ-13 catalyst over 100 h under photothermal conditions, displaying the yields of CH_3OH and CO_2 alongside CH_3OH selectivity. (d) Comparison of the CH_3OH yield and selectivity obtained in this work with other zeolite supported Cu based catalysts reported in the literature. Reaction conditions: 0.1 g catalyst, 425 °C, 300 W Xe lamp (200-400 nm), $CH_4/O_2/H_2O$ = 144/18/48 mL min^{-1}, N_2 balance, 225 mL/min in total. (e) Arrhenius plots for different catalytic systems (Cu/SSZ-13 under light, Cu/Zn-SSZ-13 in the dark, and Cu/Zn-SSZ-13 under light). (f) Comparison of the calculated apparent activation energies derived from the Arrhenius plots.

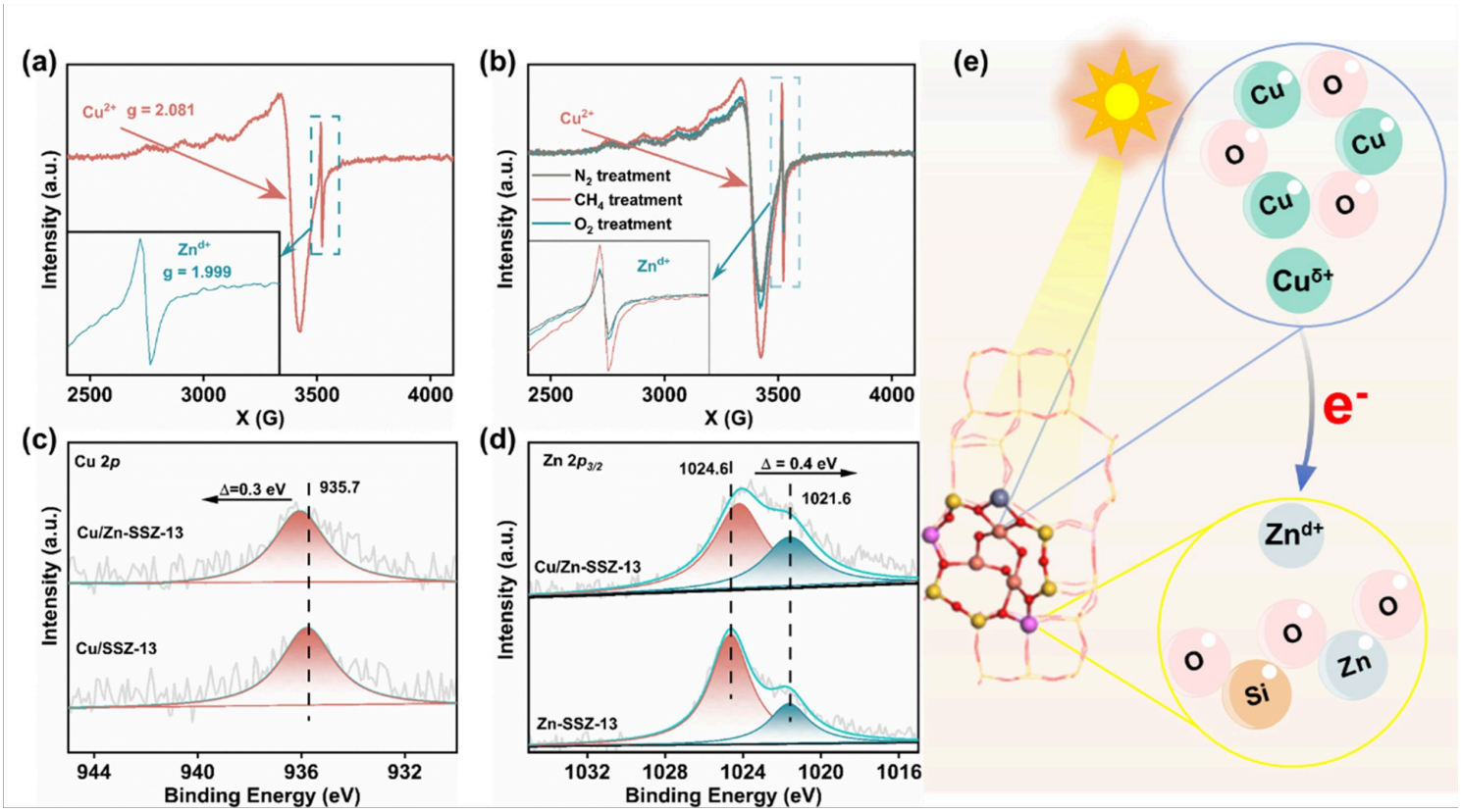


Figure 4

Electronic coupling between framework Zn and confined Cu species. (a) EPR spectrum of the Cu/Zn-SSZ-13. The inset displays the magnified signal at g = 1.999, typically assigned to Zn related spin species or defect sites. (b) EPR spectra of the Cu/Zn-SSZ-13 catalyst following treatment under different atmospheres (CH_4, O_2, and N_2). (c) High resolution Cu 2p XPS spectra of the Cu/Zn-SSZ-13 and Cu/SSZ-13 samples. (d) High resolution Zn $2p_{3/2}$ XPS spectra and the corresponding deconvolutions for the Cu/Zn-SSZ-13 and Zn-SSZ-13, (e) Charge transfer between Cu and Zn.

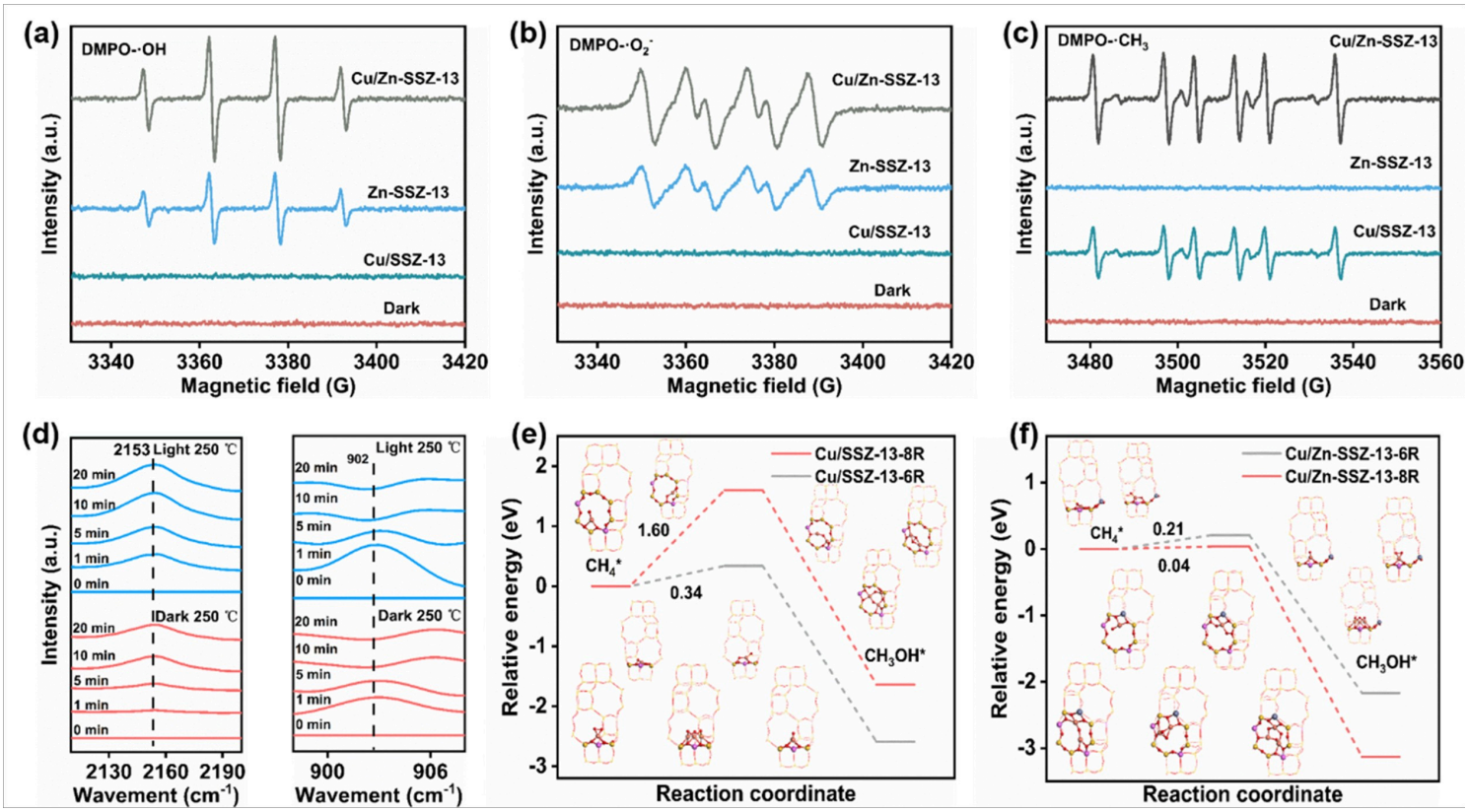


Figure 5

Mechanistic insights into Zn-enabled photothermal methane oxidation. (a-c) EPR spectra of the catalysts under various conditions using DMPO as a spin trap for (a) •OH, (b) $•O_2^-$, and (c) $•CH_3$. (d) In situ DRIFTS spectra of the Cu/Zn-SSZ-13 catalyst recorded at 250 °C under light irradiation and in the dark over time. (e, f) DFT calculated potential energy profiles for the oxidation of methane to methanol over (e) Cu/SSZ-13 and (f) Cu/Zn-SSZ-13 at the 8R and 6R locations.

Supplementary Files

This is a list of supplementary files associated with this preprint. Click to download.

- SupplementInformation.docx